Available online at www.sciencedirect.com

ScienceDirect

Geochimica et Cosmochimica Acta 266 (2019) 17–28

Geochimica et Cosmochimica Acta

www.elsevier.com/locate/gca

Modal analyses of lunar soils by quantitative X-ray diffraction analysis

G. Jeffrey Taylor [a,*], Linda M.V. Martel [a], Paul G. Lucey [a], Jeffrey J. Gillis-Davis [a], David F. Blake [b], Philippe Sarrazin [c]

[a] *Hawaii Institute of Geophysics and Planetology, School of Ocean and Earth Science and Technology, University of Hawaii, Honolulu, HI, USA*
[b] *NASA Ames Research Center, Moffett Field, CA, USA*
[c] *SETI Institute, Mountain View, CA, USA*

Received 8 February 2019; accepted in revised form 28 July 2019; available online 2 August 2019

Abstract

We used X-Ray Diffraction (XRD) and Rietveld refinement to determine the modal mineralogy of 118 lunar regolith samples (<150 μm size fraction) from all landed Apollo missions. Data were calibrated with mineral mixtures and compared to results based on an X-ray digital imaging procedure for six soils obtained by the Lunar Soil Characterization Consortium. Agreement between XRD and digital imaging for all minerals detectable in the six soils is excellent ($R^2 = 0.953$). XRD-based ternary plots (plagioclase-total pyroxene-olivine) vary from plagioclase-dominated (highlands as represented by Apollo 16 samples) to substantial mafic abundances at the mare sites. Olivine varies in relative abundance, with the Apollo 17 mare sites having the largest abundances. Olivine reaches 20 wt% at Apollo 17, but is a minor component at Apollo 14. The results agree with trends in mineral abundances obtained from reflectance spectroscopy for the Apollo sites. In a global context, however, the spectral data display a trend of increasing olivine at roughly constant pyroxene/plagioclase, reaching values of 40% olivine in the plagioclase-pyroxene-olivine ternary plot (e.g., Eratosthenian flows in Procellarum), indicating the presence of significant volumes of olivine-rich rock types on unsampled regions of the lunar surface.

Keywords: Moon; Regolith; Mineralogy; Lunar soil; Rietveld refinement; X-ray diffraction

1. INTRODUCTION

We have performed Quantitative X-Ray Diffraction (QXRD) analyses on a broad range of Apollo soil composition and maturity to provide a robust mineralogical dataset to test and improve remote sensing algorithms. Remote sensing of the lunar surface obtained by the Near Infrared Camera on the Clementine mission, Moon Mineral Mapper (M^3) on the Chandrayaan-1 mission, and the SELENE Multi-band Imager (MI) provide nearly global datasets in visible to near-infrared spectral ranges. These data can be used to determine the abundances of minerals across the lunar surface at spatial resolutions as fine as 25 meters/pixel (e.g., Lucey, 2004; Ohtake et al., 2009; Yamamoto et al., 2010, 2012; Crites and Lucey, 2015; Crites et al., 2015; Lemelin et al, 2015). However, current methods for extraction of mineralogy are hampered by the scarcity of ground-truth data for algorithm development, testing, validation, and characterization of uncertainties.

Many petrographic studies have reported modal abundances of constituents in lunar soils, but none determined the bulk mineral abundances. Instead, reported modes included assorted rock fragments, agglutinates, glass fragments, and clasts of minerals. An important exception to this is the high quality modal and chemical data available

* Corresponding author.
E-mail address: gjtaylor@higp.hawaii.edu (G.J. Taylor).

https://doi.org/10.1016/j.gca.2019.07.046
0016-7037/

through the excellent, painstaking work of the Lunar Soils Characterization Consortium (LSCC) using scanning electron microscopy (implemented in an electron microprobe) to determine mineral abundances using X-ray digital imaging combined with back-scattered electron imaging and energy dispersive spectroscopy (Taylor et al., 1996, 2001a, b, 2010). In contrast to point-counting using optical microscopy, digital imaging produces precise volume percentages (at least for the two-dimensions viewed on thin sections). However, there are some drawbacks to the LSCC database: (1) The number of analyzed soils is small (19), hampering training and testing of statistical methods (Li, 2006; Pieters et al. 2006). (2) For some key components known to vary widely (especially olivine and Mg#) the range of abundance in the LSCC data is small (e.g. olivine, 0–4 wt %), resulting in poor prediction of abundances (Li, 2006). (3) The number of immature samples is small (only five), thus hampering validation of radiative transfer methods that require the strong spectral signals in immature soil (Lucey, 2004). (4) The LSCC data do not include all the soils analyzed by Blewett et al. (1997) for Apollo and Luna sampling stations; mineral abundances for specific stations enable direct calibration of remote sensing data to abundance.

To address these problems, we made QXRD analyses of lunar soils. We use XRD rather than X-ray elemental mapping as used by the LSCC because the former method is much less time consuming than the latter, enabling collection of data for 118 soils. This approach allowed us to quantify the abundances of all minerals in these samples above a detection limit of about 0.3 wt% (see below), including those in comminuted regolith and incompletely fused agglutinates that are too fine to be quantified by optical methods. Blewett et al. (1997) studied 107 soils to produce high quality iron and titanium calibrations from Clementine data by correlating soil chemistry with individual Clementine pixels. Those soils are part of our dataset.

This paper explains the methodology and shows that the results are within uncertainties the same as those determined by the LSCC. We provide the data for all 118 soils and give an example of their utility to understanding the Apollo 16 landing site geology.

2. METHODOLOGY

We used a compact, Olympus Terra XRD instrument, which is a commercial product derived from the CheMin XRD instrument on the Curiosity Rover on Mars. The CheMin Team have demonstrated the ability to derive quantitative mineralogical results from XRD measurements using the Terra design for a wide range of compositions (Vaniman et al., 1999; Blake, 2000; Sarrazin et al., 2005a,b). The technology is unique among XRD techniques because the instrument does not require that samples be finely powdered to obtain quality diffraction patterns (Sarrazin et al., 2005b), and it uses only a small amount of sample (about 35 mg), important for preserving lunar materials. Using a sonic agitator, a coarsely powdered sample (<150 microns) is continuously agitated within the X-ray beam, thus presenting random orientations to the diffractometer over time. We received samples of the <1 mm fraction of lunar soils and dry-sieved them to <150 μm. For six samples the <150 μm fraction was wet-sieved in methanol to produce 90–150, 45–90, 25–45, 10–25, and <10 μm size fractions for comparison with data from the LSCC. Duplicate analyses of all samples were made on separate aliquots.

Terra uses a CCD (Charge-Coupled Device) to count the number and measure the x,y positions of photons diffracted from the sample. A 2-D image of all X-ray photons having the characteristic energy of the X-ray tube (CoKα) constitutes the powder X-ray diffraction pattern. The pattern is converted to a traditional 1-D intensity vs 2-Θ plot by integrating the powder patterns circumferentially about the central beam. The 2-Θ positions were calibrated using a mixture of beryl and quartz, which have invariant 2-Θ angles for their peaks. Observed maxima from the mixture range from 13.05° 2-Θ to 53.24° 2-Θ. Eleven lines were fitted to the pattern using a least squares fitting algorithm, with weighting factors for each line. An Olympus proprietary algorithm is used to integrate the 2D images into 1D plots (intensity vs 1-Θ). This program was written by Philippe Sarrazin, the architect and designer of the CheMin instrument. The CheMin 2D to 1D algorithms are based on this algorithm. MDI's commercial filmscan program was modified to incorporate the improvements used in Terra's and CheMin's algorithms. The calibration program uses 11 lines from the beryl and quartz patterns to calculate an X axis, Y axis, and sensor angle. The user runs a standard beryl-quartz mixture, enters the observed 2 theta values into an excel spreadsheet, and the X, Y and sensor angle parameters are calculated. These parameters are then entered into the instrument's parameter set. The x, y, and sensor angle parameters are included in the header for each analysis. Note that the use of the quartz-beryl mixture was for calibrating the 2-Θ positions. They were not added to the lunar soils as internal calibration standards, as often used in quantifying XRD data.

The instrument collects the data in user-specified frames (we used 20 seconds), and sums over the total number of frames collected. We found that 1000 frames were more than sufficient to obtain a high signal-to-noise XRD pattern. Analysis time is about 5 hours per sample.

X-ray diffraction of powders has the advantage that minerals are identified from their crystallographic properties. Mixtures of minerals are complicated, however, and in the past the technique was only qualitative for mineral mixtures because of a variety of problems such as microabsorption, preferred orientation of mineral grains, overlapping reflections, and the presence of amorphous phases. These problems are significantly minimized by using whole-pattern Rietveld refinement (Rietveld, 1969), as summarized by Bish and Howard (1988), Post and Bish (1989), and Bish and Post (1993). Rietveld refinement fits the entire digital powder diffraction pattern. The process is iterative, comparing the sum of weighted, squared differences in the observed and calculated XRD pattern at every 2-Θ increment. Input parameters include key crystallographic properties (unit-cell parameters, space group symmetries, site occupancies, inter-atomic distances, peak positions). Riet-

veld whole pattern fitting uses all lines of all minerals in the fit, which maximizes the use of crystallographic information and removes the effects of preferred orientation, although the Terra instrument we used minimizes that by shaking the samples at a high frequency.

2.1. Calibration: mineral abundances

We calibrated the instrument by using 12 mixtures containing 2–5 different minerals (including glass). Mixtures (Table 1) included all major lunar minerals: plagioclase, olivine, augite, orthopyroxene, pigeonite, and ilmenite, plus quartz and glass. Pigeonite was provided by Don Lindsley (Stony Brook University) and its manufacture is described in Lindsley et al. (2019). The glass was produced in the U. Hawaii experimental petrology laboratory by Jeffrey Gillis-Davis. The minerals were obtained from specimens in the U. Hawaii and NASA Ames mineral collections. All were run in the Terra XRD instrument to certify that no contaminants were present. The mixtures were made by combining weighed quantities of the <150 μm fractions in a mortar, mixing with a spatula, and grinding to homogenize the mixture. The amounts combined were only a few times the amount used in each XRD analysis, so by running each mixture twice with different aliquots and averaging the results, we are confident that the XRD patterns are representative of each mixture.

We implemented Rietveld refinement using a commercial program called Jade (Materials Data, Inc.). The Jade program assumes certain geometries, namely one like a standard diffractometer and another like a typical film, but our instrument has a somewhat different geometry, necessitating small empirical corrections. In addition, the shaking does not necessarily produce a perfectly random powder pattern and it is possible that X-ray adsorption is not taken into account completely. Thus, we did an empirical optimization of the fit on a plot of the "true" abundance (those weighed in the laboratory) versus the measured abundance determined by the observed XRD pattern and Rietveld refinement (Fig. 1). To optimize the fit to a linear correlation, we made small adjustments to the calculated abundances of plagioclase (0.85 of the observed amount), augite (1.1 times the observed amount), ilmenite (2 times the observed amount) and pigeonite (1.25 times the observed amount). These correction factors were used when determining the mineral abundances in the lunar soils. The slope is close to 1.0 with a high R^2 of 0.997, indicating a reasonable fit to the calibration mixtures. The uncertainty in the slope, calculated using the York (1968) method, is 1%. This small uncertainty is not surprising as the fit was purposely done to minimize uncertainty by applying correction factors. Two aliquots of each sample were analyzed and the mineral abundances averaged.

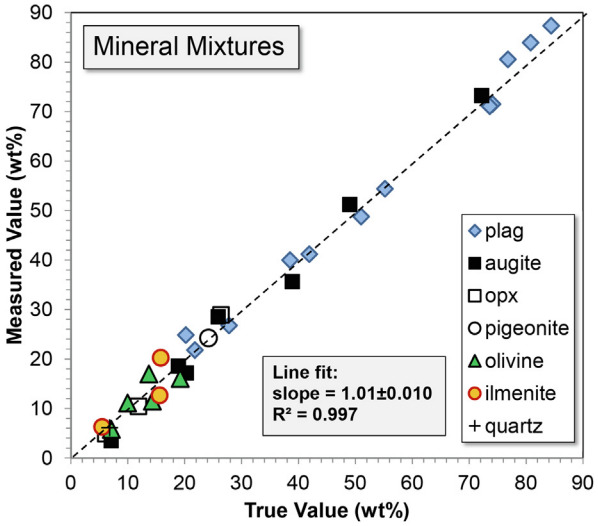

Fig. 1. Mineral abundances in mixtures of terrestrial minerals as determined by X-Ray Diffraction and Rietveld refinement versus the "true value" (the weight percentages in the mixtures). Secondary corrections to initial Rietveld refinement were made to each mineral to maximize the fit of the data to a line.

To test the calibration, we made size separates as done by the LSCC and compared our results to those of the LSCC in the 25–45 μm size fraction for six soils (Fig. 2): high-Ti and low-Ti maria, two Apollo 14 soils, and two highlands soils from Apollo 16. The data are reported on a glass-free basis. The dashed line represents the best-fit line to all the data and has a slope of 1.01 and R^2 of 0.953, indicating excellent agreement between these two independent measurements. There is more scatter below about 15 wt%, probably representing natural variation in small samples

Table 1
Mineral mixtures (weight %) used to calibrate Terra XRD instruments.

Mixture	Plagioclase	Olivine	Augite	Orthopyroxene	Pigeonite	Quartz	Ilmenite	Glass
1	51		49					
2	74.1		25.9					
3	27.8		72.2					
4	80.8	19.2						
5	84.4						15.6	
6	73.6			26.4				
7	41.9	13.7	38.9				5.5	
8	20.2	14.3	18.9			6.8		39.8
9	21.8	7.1	20.3				15.8	35
10	38.5			11.9				49.6
11	76.8	10.0	7.1	6.1				
12	55.2			20.6	24.2			

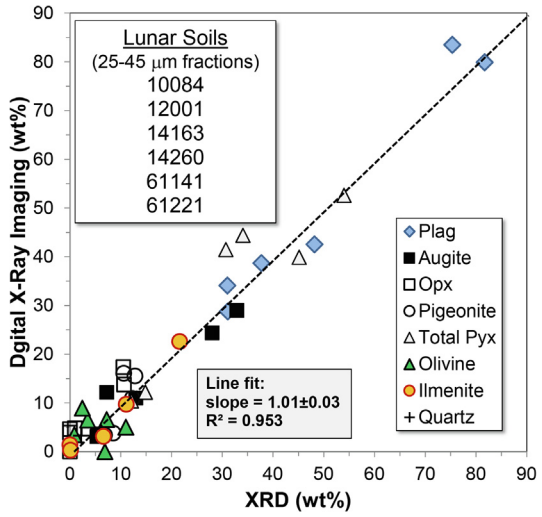

Fig. 2. XRD modal analyses versus those obtained by the digital imaging method used by the LSCC (Taylor et al., 2001a,b, 2010). LSCC data shows that mineral modal abundances vary with grain size, so this comparison is confined to the 25–45 μm fraction only. The data conform to a line with a high R^2 value. The uncertainty in the slope (±3%, 1-s) is a reasonable estimate of the average uncertainty in the measurements, though data are clearly less well-correlated for abundances <10 wt%.

taken from the soils and the inherent uncertainty in each dataset. Nevertheless, results are reasonable and for minerals with abundances greater than ~15 wt%, the agreement is very good. The uncertainty in the slope, calculated by the York (1968) least squares technique, is 3% of the slope, hence roughly 3% of the amount present for minerals more abundant that ~15 wt%. For minerals with lower abundances, the scatter in Fig. 2 indicates higher uncertainties, perhaps as much as a factor of 2 for minerals present at the <5 wt% level. Detection limits for minor minerals are about 0.3 wt%.

2.2. Calibration: glass abundances

Our measurements of amorphous materials (mainly agglutinitic glass in lunar soils) are less accurate. An important obstacle is that the abundance of glass does not use well-defined peaks in the X-Ray spectra because of the lack of long-range order in amorphous materials. Instead, amorphous materials give a broad hump due to X-ray scattering, not classic Bragg diffraction from lattice planes (Fig. 3). To calibrate the glass abundances, we used artificial glasses with compositions corresponding to green, yellow, orange, and red pyroclastic glass beads, which had been prepared by Jeffrey Gillis-Davis using a gas-mixing furnace at lunar-like oxygen fugacity (0.5 log fO_2 or IW + 1). (See the Electronic Annex for details and glass compositions.) Glass colors vary according to TiO_2 concentrations, ranging from less than 1 wt% in green glasses to 16 wt% in red glasses (Delano, 1986).

Glass XRD patterns are shown in Fig. 3. The broad hump is evident in all patterns and there is a slight shift in the peak position with TiO_2 content, the major compositional characteristic used in classifying lunar pyroclastic glasses. This shift could be caused by variation in TiO_2 or SiO_2 concentration, which ranges from 45 wt% in green glass to 35 wt% in red glass (see the Electronic Annex). This trend is supported by XRD analyses of rhyolites and other materials containing ~70 wt% SiO_2, which have broad scattering peaks at 2-Θ values of around 25 (e.g., Morris, et al., 2016). The minor peak that occurs at 19.5° 2Θ in two samples is a result of diffraction from the mylar windows in the sample cell (the other two used kapton for the cell windows, which has a 2Θ peak below the range shown).

The Jade program fits the amorphous scattering hump by using a Reference Intensity Ratio (RIR) that is input by the user. To determine the optimal value for our analyses, we fit a number of glass-mineral mixtures, varying the relative intensity ratio to get an acceptable fit to the weighed amount of the glass in each mixture. Results did not vary in any systematic way with soil composition. (Note that RIR values are not necessary for determining mineral abundances when using whole-pattern Rietveld fitting.)

We used an average relative intensity ratio of 2.4 in comparing our XRD modes with those of the LSCC for the same six soils shown in Fig. 2. In contrast to our excellent agreement with mineral abundances (on a glass-free basis), XRD glass contents for five of our six comparison soils are much lower than the values reported by the LSCC (Fig. 4). The offset may reflect an overestimate of the glass abundance by the X-ray digital imaging technique. For example, the LSCC technique used each point analysis to classify it into a mineral using the stoichiometric proportions of elements. When an analysis did not match the stoichiometry of a mineral, it was classified as a glass. Thus, any point on or within a micron or two (the diameter of the electron beam analytical volume) of a grain boundary would have been classified as a glass. In addition, agglutinates, which are the major source of glass in the lunar regolith, contain a high percentage of small mineral fragments, which would be easily mistaken for a mixture because it would be probable that the beam would be interrogating a grain boundary (including grains below the plane of a thin section). Whatever the cause of this discrepancy, the glass abundances are a secondary objective to our main goal of determining relative mineral abundances to improve our ability to extract mineral modal abundances from remote sensing reflectance data. Fortunately, even if the abundance of glass is incorrect, the relative abundances of the minerals detected will be correct (Bish and Post, 1993).

2.3. Minerals used in Rietveld refinement

Rietveld whole-pattern fitting modifies the crystallographic parameters such as unit-cell parameters (axial sizes and angles) within limits that can be set by the user. A good general description of the procedures for characterizing single phases is given by McCusker (1999) and its use in determining abundances in mixtures is described by Bish and Post (1993). Besides calculating the abundances of minerals in a mixture, Rietveld refinement also determines the average properties of each mineral, such as site occupancies and atomic positions, potentially giving compositional informa-

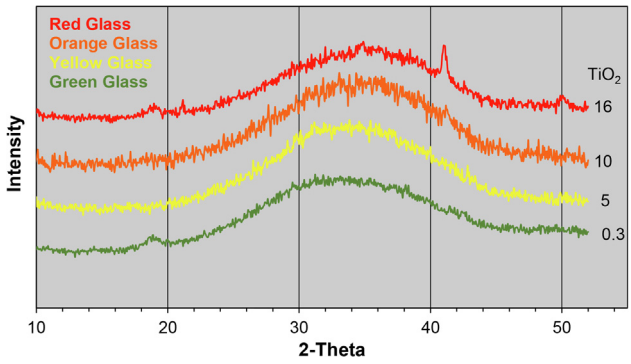

Fig. 3. X-Ray Diffraction spectra of four glass compositions. Patterns are offset, so intensities are not absolute values. TiO_2 is in wt%. All show the expected amorphous hump due to X-ray scattering.

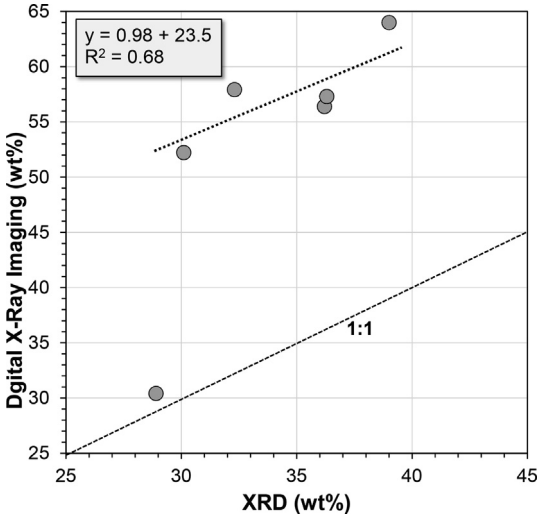

Fig. 4. Comparison of the modal glass abundance determined by XRD and point counting, for the same six soils shown in Fig. 2. Except for one point, glass abundances determined by XRD are lower than the abundance determined by digital X-ray imaging. The diagonal line shows a 1:1 fit between the two methods.

tion (e.g., forsterite content of olivine). We focused on mineral abundances. The Jade program fits all lines of each user-defined mineral in a mixture, changing the lattice parameters (within user-defined limits) to maximize the quality of the fit. For the background we used a linear fit defined by regions lacking crystallographic peaks or the broad scattering peak (Fig. 5). During data reduction we added major and minor minerals to test if their addition or deletion improved the fit between the calculated and measured XRD pattern. We report the presence of minerals at the <1 wt% level only if their addition to the mineral set improved the fit, as defined by minimization of the least squares residuals between the measured and calculated patterns. The list of minerals and sources of their crystallographic properties we used in doing Rietveld refinement and whole-pattern fitting is given in Table 2.

3. RESULTS

All data are posted at the Open Data Repository (https://odr.io/lunar-regolith-xrd). This dataset includes the 2-D images recorded with each analysis (the powder pattern), raw XRD 2-Θ data (tabular and plotted) for each run, and the average mineral and glass abundances, reported both with the glass modal abundance and on a glass-free basis. These data can be used as ground truth for remote sensing data, a major motivation for these measurements.

Two examples of XRD spectra fitted using Rietveld refinement for two mature soils (highlands soil 69,961 and mare soil 12044) are shown in Fig. 5, along with the major-element chemical compositions of the two soils. The fitted patterns are excellent, as shown by the overlaid fitted curve to the raw data and by the small amplitude variations in the difference patterns. Not surprisingly, modal mineralogy is consistent with chemical composition, as seen by higher Al_2O_3 in plagioclase-rich soil 69961 from the highlands and higher MgO and FeO in mafic-rich mare soil 12044. The highland soil contains less than detectable amounts of minor minerals such as silica polymorphs, phosphates, chromite, ilmenite. This does not mean that these minerals are absent from the Apollo 16 regolith, only that their abundances are below ~ 0.3 wt%.

4. DISCUSSION

4.1. Global perspective

Relative abundances (vol%) of plagioclase, olivine, and total pyroxene are shown in Fig. 6A. The original data in wt% have been converted to vol% in Fig. 6 for comparison with remote sensing data (Crites and Lucey, 2015). For this conversion we used densities (in g/cm^3) of 2.68 for plagioclase, 3.3 for olivine, 3.4 for augite, 3.38 for pigeonite, and 3.55 for orthopyroxene. In principle we could have used a variety of densities to account for density differences between Fe-rich pyroxene and olivine in maria and less Fe-rich mafics in the highlands. Such a procedure would be complicated because all sampled regolith is a mixture of mare, highland, and KREEP-rich basaltic rock, all of

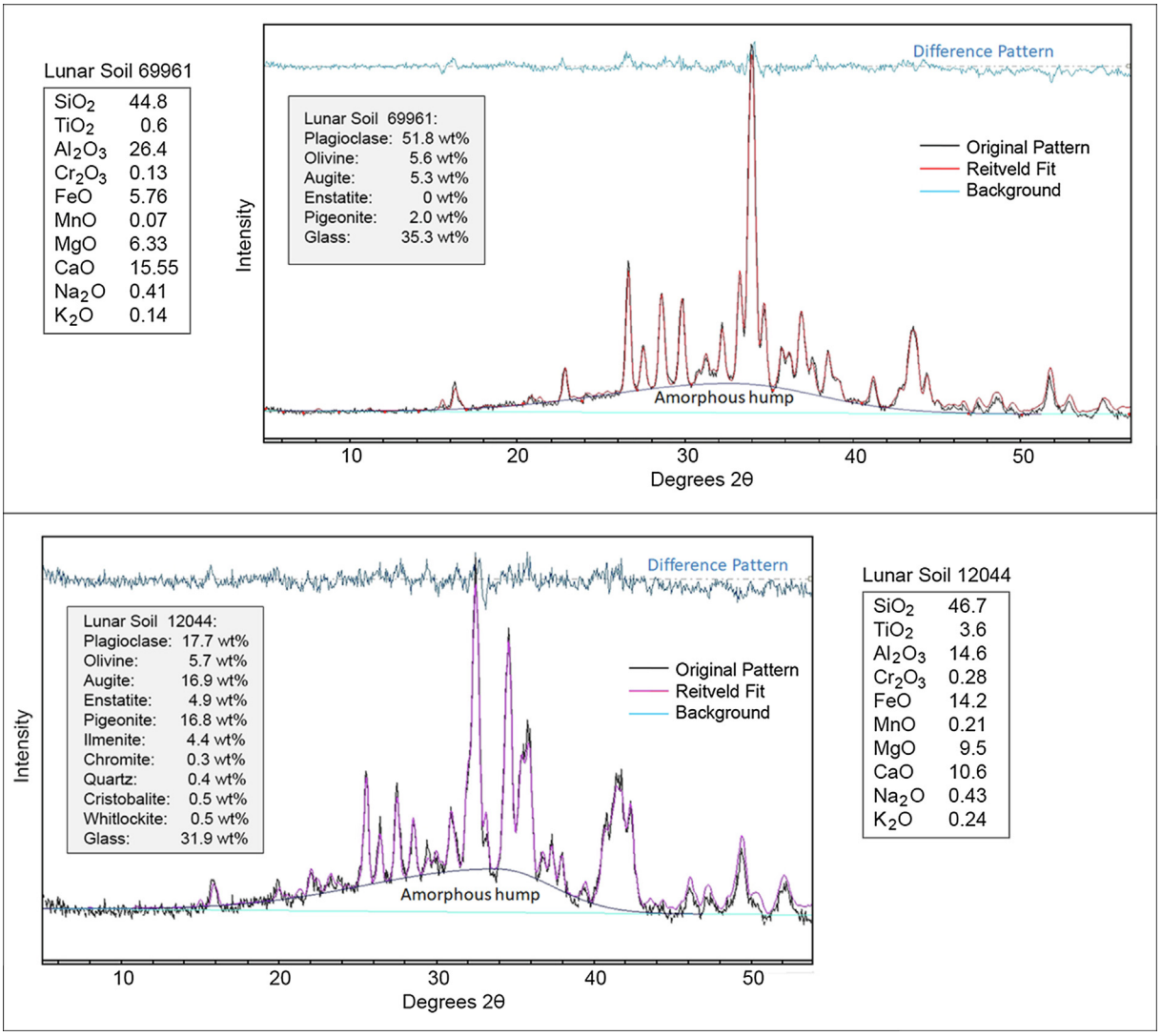

Fig. 5. Results for two lunar soils, a highlands soils from Apollo 16 (top) and a mare soil from Apollo 12, along with published chemical analyses (wt%) of bulk <1 mm soils. Fit to raw data is excellent in each case and is typical of results for all 118 soils. Chemical analyses are from Rose et al., 1973 (69961) and Frondel et al., 1971 (12044).

Table 2
Minerals used in Rietveld refinements.

Mineral	Reference for crystallographic properties
Bytownite	Chiari et al. (1984)
Forsterite	Della Giusta et al. (1990)
Augite	Gualtieri (2000)
Enstatite	Ohashi (1984)
Pigeonite	Clark et al. (1971)
Ilmenite	Shirane et al. (1959)
Armalcoite	Wechsler (1977)
Chromite	Smyth and Bish (1988)
Quartz	Wright and Lehmann (1981)
Cristobalite (low)	Nieuwenkamp (1935)
Whitlockite	Yashima et al. (2003)

which vary in Fe/Mg, hence in density. The Apollo 15 and 17 sites contain both maria and highlands, so there is a continuum of compositions. Considering the uncertainties in mineral abundances determined by XRD and remote sensing, using a single density of each mineral is acceptable for our purposes in this paper. For future work using our modal mineralogy to improve the quantification of the remote sensing data it will be essential to make such meticulous corrections. The abundances vary from plagioclase-dominated highlands, as represented by Apollo 16, to substantial mafic abundances at the mare sites. Olivine varies in relative abundance, with the Apollo 17 mare sites having the largest abundances. Olivine reaches 20% relative abundance at Apollo 17, but is a minor component in soils from the massifs at Apollo 15 and 17. Olivine is certainly an abundant mafic mineral in Mg-suite troctolites and some highland breccias, but it appears that these are not plentiful enough at the landing sites for soils to contain significantly more olivine than pyroxene among the mafic minerals. Olivine abundance appears to be bimodal at the Apollo 15 and 17 landing sites, a reflection of sampling of both highland and mare

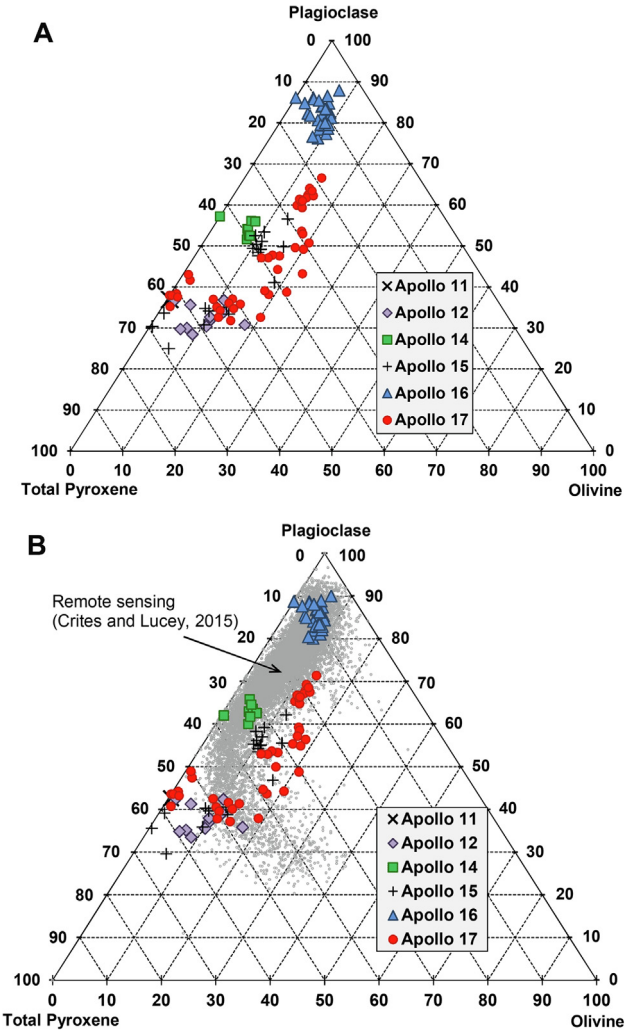

Fig. 6. Mineral abundances (vol%) of the three major mineral groups in all soils analyzed. A) Data for Apollo samples determined by XRD. Note that mafic assemblage is dominated by pyroxene. B) Same as A, but with modal abundances determined by near-global remote sensing data (2-deg pixels).

areas during those missions, coupled with variations in the olivine/pyroxene ratio among the mare basalts. Apollo 16 is distinctive because of its high plagioclase abundance and the more continuous variation in olivine/pyroxene.

A global overview of major mineral variations is given by the nearly-global remote sensing dataset obtained from Clementine spectroscopy (Crites and Lucey, 2015). Mineral abundances from spectral data are shown in Fig. 6B as gray dots, which are individual 2-deg pixels. Most of the abundances derived from remote sensing data follow the trends observed in Apollo regolith samples reported here. No Apollo soils plot in the region between ~65 and ~85% plagioclase and <10% olivine, although the remote sensing data indicate that many areas have compositions in this region of the ternary plot. The remote sensing data veer toward the olivine corner of Fig. 6B, indicating the widespread (but not abundant) presence of mafic rocks rich in olivine and to a lesser extent pyroxene in the lunar highlands.

Our laboratory measurements indicate that there appears to be considerable variation among the abundances of pyroxene species (Fig. 7). An advantage of X-ray Diffraction is that it identifies mineral crystal structures directly, so does not rely on inferring mineralogy from composition. Our data suggest that pigeonite is present in almost all samples, and particularly abundant (among the pyroxenes) in many Apollo 16 regolith samples. However, the Terra instrument we used has a 2-Θ resolution of about 0.3° (FWHM), which may not be sufficient to deconvolve overlapping pyroxene peaks. When we fitted X-ray spectra using the Rietveld method, the fit improved when pigeonite was added to the mixture and removing orthopyroxene usually had little effect on the quality of the fit, implying that pigeonite is present and usually more abundant than orthopyroxene. Our comparison with the LSCC results (Fig. 2) indicates reasonable agreement, but the LSCC identification of pyroxene phases were made on the basis of composition, not crystallography, so the agreement could be coincidental. Thus, we caution that the relative abundances of pyroxene phases are uncertain. The uncertainty could be removed by additional X-ray analyses using an

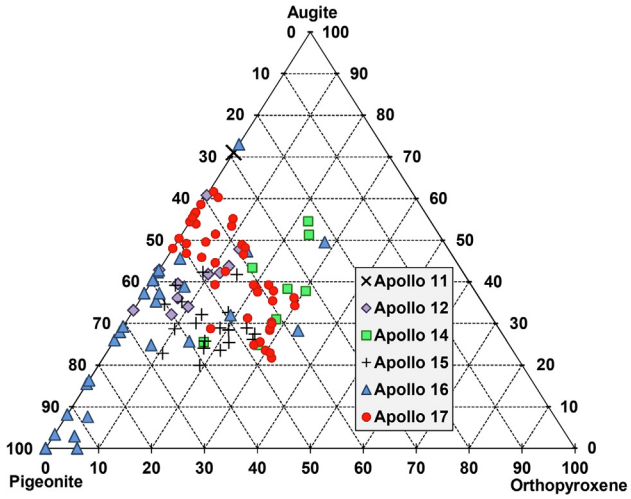

Fig. 7. Modal abundances among pyroxene species as determined by XRD. Pigeonite appears more abundant than orthopyroxene, but 2-Θ resolution of the Terra instrument limits the confidence in species abundances.

instrument with a better 2-Θ resolution. However, the overall agreement with the LSCC data indicates that the modal abundances of total pyroxene are reasonable.

The relative abundance of pigeonite and orthopyroxene is important because spectral reflectance techniques cannot distinguish pigeonite from orthopyroxene, so remote sensing results report only total low-Ca pyroxene. Bearing in mind the uncertainty in the abundances of individual pyroxenes, it appears that pigeonite is generally more abundant than orthopyroxene in the Apollo sample set, including at the Apollo 16 landing site. If correct, the higher abundance of pigeonite compared to orthopyroxene in Apollo 16 regolith suggests the presence of rocks that cooled fast enough to prevent inversion of the pigeonite to orthopyroxene with augite exsolution lamellae. The greater abundance of pigeonite compared to orthopyroxene is consistent with petrologic studies of the Apollo 16 landing site (e.g., Taylor et al., 1973; Vaniman and Papike, 1980), which indicate the presence of abundant impact melt breccias, especially on the Cayley Plains. The presence of pigeonite might also imply formation in thin sills or dikes, or lava flows, but because of the pervasive cratering in the lunar highlands, the occurrence of pigeonite most likely indicates formation in impact melt breccias, such as the poikilitic melt breccias in Apollo 16 soils. Global reflectance measurements of mineral abundances show that low-Ca pyroxenes are more abundant than olivine (e.g., Pieters, 1986; Lucey et al., 2014). Melosh et al. (2017) show that low-Ca pyroxene is the dominant mafic mineral in ejecta from the South Pole – Aiken basin, and interpreted this as an indication that excavated mantle at SPA was dominated by orthopyroxene. This interpretation is complicated by the possibility that the low-Ca pyroxene is mostly pigeonite, as it appears to be at Apollo 16 (especially in the Cayley Plains, below). Similarly, the Chang'E-4 rover mission to the lunar farside crater Von Kármán, which is within the South Pole – Aitken (SPA) basin, found by analysis of reflectance spectra that the mafic components in the regolith near the landing site contained a mixture of low-Ca pyroxene and olivine (Li et al, 2019). It will be important to determine if the low-Ca pyroxene is orthopyroxene or pigeonite. The latter would suggest a significant contribution from impact melts or a previously-unidentified lava type. The impact melts could be derived from melting of the mantle beneath SPA, but the observed low-Ca pyroxene may not represent pristine orthopyroxene from the mantle.

4.2. 4.2 Understanding the Landing Sites: Example, Apollo 16

Besides providing ground truth for remote sensing measurements, a motivation for the present work was to reassess the geological histories of the Apollo landing sites, and to put them into a regional context. We have begun this effort (Sun et al., 2018) and intend to make detailed studies that integrate our mineralogical results with geological, sample chemistry, and remote sensing data. In this section we present an overview of the Apollo 16 site based on published geological and geochemical studies and use our XRD results to test those observations.

The Apollo 16 landing site is in the southern nearside highlands, the only mission to land in the feldspathic highlands. The rationale for selecting the site was explained by Muehlberger et al. (1980), who also summarized interpretations for the origin of the two main geologic units. The site resides on the boundary between the Descartes Mountains, a large, rugged deposit of feldspathic material that occurs to the east and south of the landing site (Fig. 8), and the Cayley Plains, a smoother unit that fills low regions throughout the highlands. A major question is how much of the material at the Apollo 16 landing site was contributed by impact basins (e.g., Petro and Pieters, 2006) and how much (and which) material is reworked local rock (e.g., Oberbeck, 1975; Head, 1974). Discussion has focused on basins thought to have delivered the most material, namely Nectaris to the east and Imbrium and Serenitatis to the northwest. These two ways of viewing the landing site composition and geologic evolution are not mutually exclu-

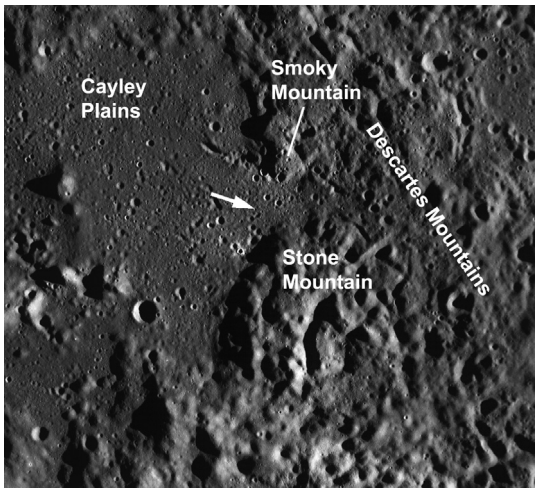

Fig. 8. Wide Angle Camera monochrome mosaic of the Apollo 16 landing site taken with the Wide Angle Camera on the Lunar Reconnaissance Orbiter Camera. Large, regional geologic units are the smooth Cayley Plains and Descartes Mountains surrounding the landing site (arrow indicates location of the lunar module). The Descartes Mountains were sampled at stations on Stone Mountain and Smoky Mountain. Image M116215423M, scene width is 65 km [NASA/GSFC/Arizona State University].

sive as the deposition of basin ejecta at the Apollo 16 landing site would have reworked the local materials. How much reworking is model dependent, but in their analysis of basin ejecta and the extent of mixing at the Apollo 16 site, Petro and Pieters (2006) conclude that there must have been substantial mixing of basin ejecta and local material.

How do our XRD mineral abundances fit into this picture? One test of the extent of mixing is the variability of mineral modal abundances throughout the site, particularly the difference between the Cayley Plains and the Descartes formation. Apollo 16 astronauts collected samples from ten stations. Three were from the Descartes Mountains (specifically the lower slope of Smoky Mountain, stations 11 and 13, and Stone Mountain, station 4). The remainder were from the Cayley Plains, although station 5 was close to the boundary between Stone Mountain and the Cayley Plains. Data and mixing calculations by Korotev (1996, 1997) and a detailed analysis of the role of basin ejecta deposited at the site (Petro and Pieters, 2006) suggest the presence of highly feldspathic ancient rock, particularly abundant in the Descartes samples, and a more mafic component deposited in the Cayley Plains. The relatively narrow range in chemical compositions of mature soils on the Cayley Plains indicates deposition by the Imbrium basin (Korotev, 1996, 1997) or by thorough mixing of Imbrium, Serentatis, and Nectaris ejecta. Concentrations of incompatible elements indicate a significant KREEP component in the Cayley Plains, and much less so in the Descartes Mountains.

Abundances (in wt%) of olivine, total pyroxene, and plagioclase (glass-free basis) are shown in Fig. 9. Mineral abundances are not drastically different throughout the site, but the Descartes sites (stations 4, 11, and 13) are marginally higher in plagioclase than all but one sampling locale on the Cayley Plains. The Descartes samples contain 83–84 wt% plagioclase, whereas the Cayley Plains sites contain 78–81 wt% (except for the LM station, which contains 84 wt% plagioclase). The olivine/pyroxene ratio for the Cayley stations ranges widely, from 0.2 to 0.8. The three Descartes stations are confined to the upper part of the Cayley range, 0.6–0.8. Pyroxene is more abundant than olivine in all samples (Fig. 9).

The Cayley Plains are distinctly richer in the KREEP components (Korotev, 1996, 1997). This is illustrated in Fig. 10, which shows the abundance of Sm (an incompatible element associated with KREEP) *versus* total pyroxene. Pyroxene abundance in the Cayley Plains and Descartes Mountains overlap considerably (also see Fig. 9), but the Cayley samples tend to have higher Sm concentrations. The higher Sm is consistent with the modal abundances of poikilitic KREEP impact melt breccias in the regolith on the Cayley Plains (45%) compared to the Descartes Mountains (25%, Taylor et al., 1973, Drake et al., 1974). Mixing calculations by Korotev (1997) show that the Cayley samples have a large contribution of KREEP-rich samples. Korotev (1997) suggests that this indicates derivation of the Cayley Plains as ejecta from Imbrum, which is located in the Procellarum KREEP Terrane. Modeling by Petro and Pieters (2006) indicates that contributions of ejecta from Serentatis and Nectaris are also likely. Our data do not help narrow down the contributions from each basin. However, taken together, all geological, chemical, petrologic, and mineralogical studies of the Apollo 16 landing site indicate the presence of an ancient feldspathic crust that has been overlain and mixed with materials ejected from large basins. It is not clear what sampling strategy would allow us to determine the relative abundances of ejecta from Imbrium, Serentatis, Nectaris, Orientale, and other basins. Perhaps additional remote sensing studies of the entire lunar highlands will help unravel this complicated geologic history.

4.3. Implications for Instruments on Landed Missions

Our results on 118 Apollo soil samples have several implications for instrument design and capability. First, as proved by the CheMin instrument on the Curiosity rover for Mars and by our analyses of lunar regolith, useful mineralogical information can be obtained by *in situ* X-Ray Diffraction. All major minerals can be identified and their abundances quantified. Minor phases (those making up less than ~5 wt% of a sample) can be detected, but their quantification is much less accurate than for major minerals. Second, an XRD instrument requires sufficient 2-Θ resolution to be able to determine the abundances of the three pyroxene phases (augite, orthopyroxene, and pigeonite). The 2-Θ resolution needs to be better than the 0.3° (FWHM) of the Terra instrument we used. Third, as Fig. 10 shows, it is important to obtain bulk chemical data as well as mineralogical data. Thus, a combination X-Ray Fluorescence (XRF) and X-Ray Diffraction (XRD) instrument would be effective, such as the Extraterrestrial Regolith Analyzer for Lunar Soil (XTRA) described by Blake et al. (2019). XTRA combines XRD with XRF to provide bulk mineralogy and chemical composition.

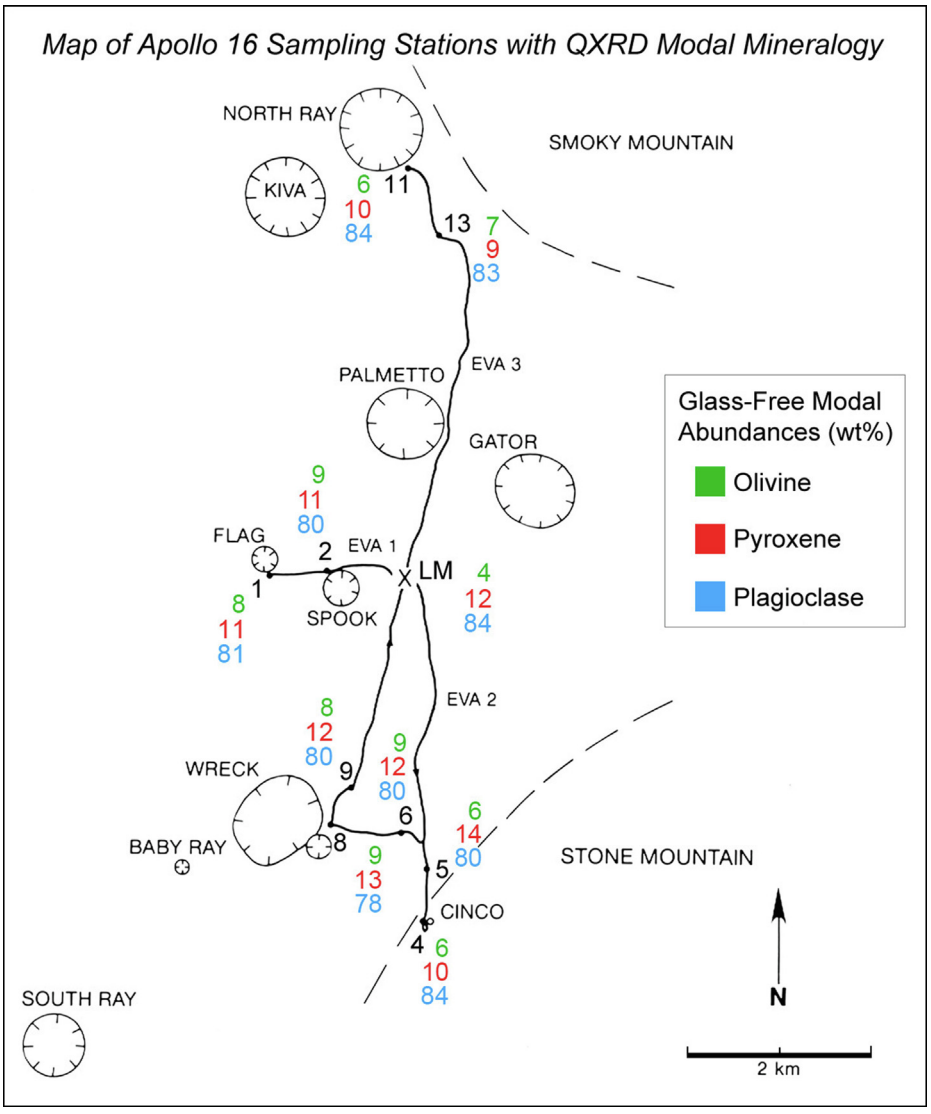

Fig. 9. Modal abundances of main silicate minerals at the Apollo 16 landing site, normalized to 100%. Sites on North Ray Crater on Smokey Mountain (stations 11 and 13) and at Stone Mountain (station 4) are slightly richer in plagioclase than the other sites, which are located on the Cayley Plains, implying a compositional difference between the Descartes Mountains (Fig. 8) and the Cayley Plains. Olivine/pyroxene ratios vary considerably, though on average are higher in the Descartes samples.

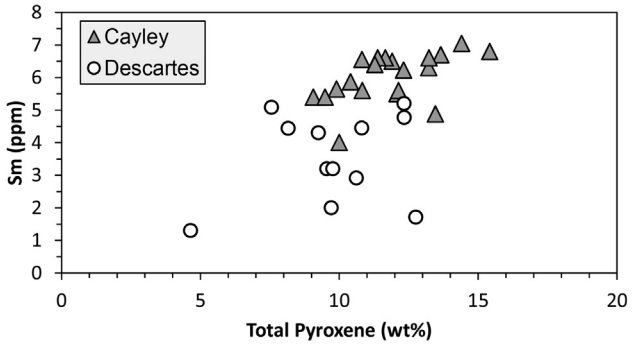

Fig. 10. Abundances of total pyroxene plotted against the Sm concentration in the same soils. Sm is associated with the KREEP component and is richer on average in the Cayley Plains than in the Descartes Mountains.

5. CONCLUSIONS

Mineral abundances determined on 118 lunar soils from all Apollo landed missions lead to the following conclusions:

1. Mineral abundances vary among the landing sites, as expected. Plagioclase is dominant at the Apollo 16 site, the best representative of the lunar highlands and much lower on the maria. Apollo 14, the Apennine Front at Apollo 15, and the massifs at Apollo 17 are intermediate in plagioclase abundance between the highlands and the maria.
2. Olivine varies in relative abundance, with the Apollo 17 mare sites having the largest abundances. Olivine reaches 20 wt% at Apollo 17, but is a minor component at Apollo 14.
3. The results agree with trends in mineral abundances obtained from reflectance spectroscopy for the Apollo sites. In a global context, however, the spectral data display a trend of increasing olivine at roughly constant pyroxene/plagioclase, reaching values of 40% olivine in the plagioclase-pyroxene-olivine ternary plot (e.g., Eratosthenian flows in Procellarum), indicating the presence of significant volumes of olivine-rich rock types on unsampled regions of the lunar surface.
4. The Descartes Mountains and Cayley Plains at the Apollo 16 landing site are distinctly different in their concentrations of incompatible trace elements, but are only marginally different in mineral abundances (the Descartes Mountains are slightly higher in plagioclase). The olivine/pyroxene ratio for the Cayley stations ranges widely, from 0.2 to 0.8, but the Descartes soils have olivine confined to the upper range of the Cayley soils, 0.6–0.8. The distinct difference between the Cayley Plains in trace element abundances coupled with the more modest differences in mineral abundances shows that it is useful for future missions to include instruments that can measure both elemental and mineralogical abundances.

ACKNOWLEDGEMENT

We are grateful to Larry Taylor for discussions of lunar soils and determination of their mineral abundances, which included both encouragement and hard questions. We thank Don Lindsley for providing samples of laboratory-produced pigeonite. Reviews by Yang Liu, two anonymous reviewers, and associate editor James Day improved the manuscript substantially. This research was supported by the NASA LASER program, grant number NNX11AE85G, and NASA Cooperative agreement 80NSSC19M0137.

RESEARCH DATA

https://odr.io/lunar-regolith-xrd.

APPENDIX A. SUPPLEMENTARY MATERIAL

Supplementary data to this article can be found online at https://doi.org/10.1016/j.gca.2019.07.046.

REFERENCES

Blake D. (2000) Remote X-ray diffraction and X-ray fluorescence analysis on planetary surfaces. *Adv. X-Ray Anal.* **43**, 487–496.

Blake D. F. et al. (2019) XTRA: an extraterrestrial regolith analyzer for lunar soil. *Lunar Planet. Sci. Conf. 50th*, abstract # 1144.

Blewett D. T., Lucey P. G., Hawke B. R. and Jolliff B. L. (1997) Clementine images of the lunar sample-return stations: refinement of FeO and TiO_2 mapping techniques. *J. Geophys. Res. Planets* **102**, 16319–16325. https://doi.org/10.1029/97JE01505.

Bish D. L. and Howard S. A. (1988) Quantitative phase analysis using the Rietveld method. *J. Appl. Cryst.* **21**, 86–91. https://doi.org/10.1107/S0021889887009415.

Bish D. L. and Post J. E. (1993) Quantitative mineralogical analysis using the Rietveld full-pattern fitting method. *Amer. Min.* **78**, 932–940.

Chiari G., Benna P. and Bruno E. (1984) The structure of bytownite (An85). *Zeit. Krist.* **169**, 35–49.

Clark J. R., Ross M. and Appleman D. (1971) Crystal chemistry of a lunar pigeonite. *Am. Mineral.* **56**, 888–908.

Crites S. T. and Lucey P. G. (2015) Revised mineral and Mg# maps of the Moon from integrating results from the Lunar Prospector neutron and gamma-ray spectrometers with Clementine spectroscopy. *Amer. Min.* **100**, 973–982.

Crites S. T., Lucey P. G. and Taylor G. J. (2015) The mafic component of the lunar crust: contraints on the crustal abundance of mantle and intrusive rock, and the mineralogy of lunar anorthosites. *Amer. Min.* **100**, 1708–1716.

Delano J. W. (1986) Pristine lunar glasses: Criteria, data, and implications. Proc. Lunar Planet. Sci. Conf., 16th, Part 2. *J. Geophys. Res.* **91**, D201–D213.

Della Giusta D., Ottonello G. and Secco L. (1990) Precision estimates of interatomic distances using site occupancies, ionization potentials and polarizability in Pbnm silicate olivines. *Acta Cryst.* **B46**, 160–165. https://doi.org/10.1107/S0108768189012322.

Drake M. J., Taylor G. J. and Goles G. G. (1974) Descartes Mountains and Cayley Plains: composition and provenance. *Proc. Lunar Sci. Conf.* **5th**, 991–1008.

Frondel C., Klein C. and Ito J. (1971) Mineralogical and chemical data on Apollo 12 lunar fines. *Proc. Second Lunar Sci. Conf.*, 719–726.

Gualtieri A. F. (2000) Accuracy of XRPD QPA using the combined Rietveld-RIR method. *J. Appl. Cryst.* **33**, 267–278. https://doi.org/10.1107/S002188989901643X.

Head J. W. (1974) Stratigraphy of the Descartes region (Apollo 16): implications for the origin of samples. *The Moon* **11**, 77–99. https://doi.org/10.1007/BF01877795.

Korotev R. L. (1996) On the relationship between the Apollo 16 ancient regolith breccias and feldspathic fragmental breccias, and the composition of the prebasin crust in the Central Highlands of the Moon. *Meteor. Planet. Sci.* **31**, 403–412.

Korotev R. L. (1997) Some things we can infer about the Moon from the composition of the Apollo 16 regolith. *Meteor. Planet. Sci.* **32**, 447–478.

Lemelin M., Lucey P. G., Song E. and Taylor G. J. (2015) Lunar central peak mineralogy and iron content using the Kaguya Multiband Imager: reassessment of the compositional structure of the lunar crust. *J. Geophys. Res. Planets* **120**, 869–887. https://doi.org/10.1002/2014JE004778.

Li C. et al. (2019) Chang'E-4 initial spectroscopic identification of lunar far-side mantle-derived materials. *Nature* **569**. https://doi.org/10.1038/s41586-019-1189-0.

Li L. (2006) Partial least squares modeling to quantify soil composition with hyperspectral reflectance measurements. *J. Geophys. Res. Planets* **111**, E04002. https://doi.org/10.1029/2005JE002598.

Lindsley D., Nekvasil H. and Glotch T. D. (2019) Synthesis of pigeonites for spectroscopic studies. *Am. Mineral.* **104**, 615–618.

Lucey P. G. (2004) Mineral maps of the Moon. *Geophys. Res. Lett.* **31**, L08701. https://doi.org/10.1029/2003GL019406.

Lucey P. G., Norman J. A., Crites S. T., Taylor G. J., Hawke B. R., Lemelin M. and Melosh H. J. (2014) A large spectral survey of small lunar craters: implications for the composition of the lunar mantle. *Amer. Min.* **99**, 2251–2257.

McCusker L. B., Von Dreele R. B., Cox D. E., Louër D. and Scardi P. (1999) Rietveld refinement guidelines. *J. Appl. Cryst.* **32**, 36–50. https://doi.org/10.1107/S0021889898009856.

Melosh H. J., Kendall J., Horgan B., Johnson B. C., Bowling T., Lucey P. G. and Taylor G. J. (2017) South Pole-Aitken basin ejecta reveal the Moon's upper mantle. *Geology* **45**, 1063–1066. https://doi.org/10.1130/G39375.1.

Morris R. V., Vaniman D. T., Blake D. F., Gellert R., Chipera S. J., Rampe E. B., Ming D. W., Morrison S. M., Downs R. T., Treiman A. H., Yen A. S., Grotzinger J. P., Achilles C. N., Bristow T. F., Crisp J. A., Des Marais D. J., Farmer J. D., Fendrich K. V., Frydenvang J., Graff T. G., Morookian J.-M., Stolper E. M. and Schwenzer S. P. (2016) Silicic volcanism on Mars evidenced by tridymite in high-SiO_2 sedimentary rock at Gale crater. *PNAS* **113**, 7071–7076. https://doi.org/10.1073/pnas.1607098113.

Muehlberger W. R., Hörz F., Sevier J. R. and Ulrich G. E. (1980) Mission objectives for geological exploration of the Apollo 16 landing site. *Proc. Conf. Lunar Highlands Crust*, 1–49.

Nieuwenkamp W. (1935) Die Kristallstruktur des Tief-Cristobalits SiO2. *Zeit f Krist.* **82**, 82–88.

Oberbeck V. R. (1975) The role of ballistic erosion and sedimentation in lunar stratigraphy. *Rev. Geophys.* **13**, 337–362. https://doi.org/10.1029/RG013i002p00337.

Ohashi Y. (1984) Polysynthetically-twinned structures of enstatite and wollastonite. *Phys. Chem. Minerals* **10**, 217–229. https://doi.org/10.1007/BF00309314.

Ohtake M. et al. (2009) The global distribution of pure anorthosite on the Moon. *Nature* **461**, 236–240. https://doi.org/10.1038/nature08317.

Petro N. E. and Pieters C. M. (2006) Modeling the provenance of the Apollo 16 regolith. *J. Geophys. Res. Planets* **111**, E09005. https://doi.org/10.1029/2005JE002559.

Pieters Carle M. (1986) Composition of the lunar highland crust from near-infrared spectroscopy. *Rev. Geophys.* **24**(3), 557–578. https://doi.org/10.1029/RG024i003p00557.

Pieters C. M., Shkuratov Y., Kaydash V., Stankevich D. and Taylor L. A. (2006) Lunar soil characterization consortium analyses: pyroxene and maturity estimates derived from Clementine image data. *Icarus* **184**, 83–101. https://doi.org/10.1016/j.icarus.2006.04.013.

Post J. E. and Bish D. L. (1989) Rietveld refinement of crystal structures using powder X-ray diffraction data. *Rev. Mineral.* **20**, 277–308.

Rietveld H. M. (1969) A profile refinement method for nuclear and magnetic structures. *J. Appl. Crystallogr.* **2**, 65–71.

Rose H. J., Cuttitta F., Berman S., Carron M. K., Christian R. P., Dwornik E. J., Greenland L. P. and Ligon D. T. (1973) Compositional data for twenty-two Apollo 16 samples. In *Proc. 4th Lunar Sci. Conf.*, pp. 1149–1158.

Sarrazin P., Blake D., Feldman S., Chipera S., Vaniman D. and Bish D. (2005a) Field deployment of a portable XRD/XRF instrument on Mars analog terrain. *Powder Diffr.* **20**, 128–133. https://doi.org/10.1154/1.1913719.

Sarrazin P., Chipera S., Bish D., Blake D. and Vaniman D. (2005b) Vibrating sample holder for XRD analysis with minimal sample preparation. *Adv. X-Ray Anal.* **48**, 156–164.

Shirane G., Pickart S. J., Nathans R. and Ishikawa Y. (1959) Neutron-diffraction study of antiferromagnetic $FeTi0_3$ and its solid solutions with α-Fe_2O_3. *J. Phys. Chem. Solids* **10**, 35–43.

Smyth J. R. and Bish D. L. (1988) Crystal Structures and Cation Sites of the Rock-Forming Minerals. Allen and Unwin, Boston.

Sun L., Taylor G. J., Martel L. M. V. and Lucey P. G. (2018) A comprehensive study of mineralogy at Apollo 17 landing site. *49th Lunar Planet. Sci. Conf.*, #1693(abstr.).

Taylor G. J., Drake M. J., Hallam M. E., Marvin U. B. and Wood J. A. (1973) Apollo 16 stratigraphy: the ANT hills, the Cayley Plains, and a pre-Imbrian regolith. In *Proc. Lunar Sci. Conf. 4th*, pp. 553–568.

Taylor L. A., Patchen A., Taylor D. H. S., Chambers J. G. and McKay D. S. (1996) X-ray digital imaging petrography of lunar mare soils: modal analyses of minerals and glasses. *Icarus* **124**, 500–512.

Taylor L. A., Pieters C., Keller L. P., Morris R. V., McKay D. S., Patchen A. and Wentworth S. (2001a) The effects of space weathering on Apollo 17 mare soils: petrographic and chemical characterization. *Meteor. Planet. Sci.* **36**, 285–299. https://doi.org/10.1111/j.1945-5100.2001.tb01871.x.

Taylor L. A., Pieters C. M., Keller L. P., Morris R. V. and McKay D. S. (2001b) Lunar mare soils: space weathering and the major effects of surface-correlated nanophase Fe. *J. Geophys. Res. Planets* **106**, 27985–27999. https://doi.org/10.1029/2000JE001402.

Taylor L. A., Pieters C., Patchen A., Taylor D.-H. S., Morris R. V., Keller L. P. and McKay D. S. (2010) Mineralogical and chemical characterization of lunar highland soils: insights into the space weathering of soils on airless bodies. *J. Geophys. Res. Planets* **115**, E02002. https://doi.org/10.1029/2009JE003427.

Vaniman D. and Papike J. J. (1980) Lunar highland melt rocks: chemisry, petrology and silicate mineralogy. In *Proc. Conf. Lunar Highlands Crust*, pp. 271–337.

Vaniman D., Bish D., Guthrie G., Chipera S., Blake D., Collins S. A., Elliott S. T. and Sarrazin P. (1999) *Process monitoring and control with CHEMIN, a miniaturized CCD-based instrument for simultaneous XRD/XRF analysis*. Penetrating Radiation Systems and Applications, pp. 243–251.

Wechsler B. A. (1977) Cation distribution and high-temperature crystal chemistry of armalcolite. *Amer. Mineral.* **62**, 913–920.

Wright A. F. and Lehmann M. S. (1981) The structure of quartz at 25 and 590°C determined by neutron diffraction. *J. Solid State Chem.* **36**, 371–380. https://doi.org/10.1016/0022-4596(81)90449-7.

Yamamoto S., Nakamura R., Matsunaga T., Ogawa Y., Ishihara Y., Morota T., Hirata N., Ohtake M., Hiroi T., Yokota Y. and Haruyama J. (2010) Possible mantle origin of olivine around lunar impact basins detected by SELENE. *Nat. Geosci.* **3**, 533–536. https://doi.org/10.1038/NGEO897.

Yamamoto S., Nakamura R., Matsunaga T., Ogawa Y., Ishihara Y., Morota T., Hirata N., Ohtake M., Hiroi T., Yokota Y. and Haruyama J. (2012) Massive layer of pure anorthosite on the Moon. *Geophys. Res. Lett.* **39**, L13201. https://doi.org/10.1029/2012GL052098.

Yashima M., Sakai A., Kamiyama T. and Hoshikawa A. (2003) Crystal structure analysis of β-tricalcium phosphate $Ca_3(PO_4)_2$ by neutron powder diffraction. *J. Solid State Chem.* **175**, 272–277. https://doi.org/10.1016/S0022-4596(03)00279-2.

York D. (1968) Least squares fitting of a straight line with correlated error. *Earth Planet. Sci. Lett.* **5**, 320–324. https://doi.org/10.1016/S0012-821X(68)80059-7.

Associate editor: James M.D. Day